# Accuracy of Global Geospace Simulations: How much of the error arises from solar wind input uncertainties?

**Q. Al Shidi[1], T. I. Pulkkinen[1], D. Welling[1], G. Toth[1]**

[1]University of Michigan, Department of Climate & Space Sciences and Engineering

**Key Points:**

- The phase front normal used to propagate the solar wind contributes to the error variance of the geomagnetic indices.
- The simulation produces a larger error variance during stronger solar wind driving than those arising from the solar wind propagation method.
- Simulation output confidence is best for phase front normals smaller than $> 0.4$.

Corresponding author: Qusai Al Shidi, qusai@umich.edu

## Abstract

In this study, we examine the accuracy of global geospace simulations by analyzing the relationship between the solar wind and its propagation parameters and the errors in auroral electrojet index AU and AL, ring current index SYM-H and the cross-polar cap potential (CPCP) in simulations. We show that generally the error distributions are wider for higher level of solar wind driving. Our results also show that the observing solar wind monitor distance from the Sun-Earth line and the phase front normal angle produce only minor effects on the error distributions, however, for oblique angles (¡0.4) of the phase front normal there are noticable effects on the error distributions. Furthermore, we show that the results hold true also when using two magnetometer station recordings, one at subauroral and the other at auroral latitudes, which speak to the similarity of the error sources in local and global activity measures. These results are important elements in assessing the accuracy of the timing and magnitude of space weather events recorded on ground.



## Plain Language Summary

We investigate the accuracy of solar wind data that is predicted on arrival to the Earth. We do this by comparing geomagnetic storm indices in our simulations to the observed indices. We show that the strength of the solar wind gives us a wider difference in the index in question than the parameters used to predict the solar wind at Earth. We show that for oblique angles in the magnetic field configuration there are effects on this difference, but not a noticable one if the solar wind observing spacecraft is far off the Sun-Earth axis.


## 1 Introduction

Global simulations of Geospace are numerous. They are used to answer science questions and for operational use in order to forecast geomagnetic indices. Typically, these simulations use data from satellites that orbit at the first Lagrange point (L1) and propagated to somewhere closer to the bow-shock nose (BSN). This is to avoid running a physics based simulation that run from L1 to the BSN. L1 to BSN propagation time delays methods see operational use for space weather forecasting (Cash et al., 2018).

Magnetohydrodynamic (MHD) simulations of Geospace has its limitations. Generally, these models use ideal MHD (Lyon et al., 2004; Janhunen et al., 2012; Gombosi et al., 2021). Which approximates the solar wind and magnetosphere plasma as a single-fluid, without any viscosity or dissipative terms in its governing equations. These simulations are also limited to the resolution in which it was run. A certain numerical scheme must be employed to solve these governing equations and depending on the choice can be diffusive or dispersive. Solving these equations can cause magnetic monopoles to arise simply due to discretization. These simulations, especially in the case of this study, are highly coupled with other models with their own limitations. Coupling models is necessary to resolve different regimes in space weather, this is because different parts of the global system has differing time scales . These approximations, limitations, and numerical issues can lead to errors when compared to observations.

This is not to say that observations are perfect either, there are measurement uncertainties with any kind of instrument. Fundamentally, measurements have systematic errors and random errors. Instruments also have their own accuracy, precision and range. These errors and uncertainties if used as an input to a model can be forward-propagated to the output of the model.

This leads us to errors in the output of models as compared to observations. Errors in data input and model limitations can lead to errors in the output. Thus, it is im-

portant to validate models with observations with some confidence interval. We may imagine a measurement from a model or observation to be a probability distribution function and study its properties.

Solar wind propagation has several sophisticated methods to determine the time delays of the solar wind observation. They use methods to determine the Phase Front Normal (PFN) plane of the solar wind during the observation and calculating the time shift along this normal. These methods have been extensively validated and studied and they include Minimum Variance Analysis (MVA) (Sonnerup & Scheible, 1998), the cross-product technique (Horbury et al., 2001), and a combination of the two (Weimer & King, 2008).

Investigations have been done on the past studying solar wind propagation methods with global simulations (A. Pulkkinen & Rastätter, 2009). As well as solar wind propagation from the L1 monitor towards an auroral response in R0 currents (Milan et al., 2022). This study will take a look at how those methods affect our prediction of geomagnetic indices.

With the increase of computing power comes capabilities to apply statistical methods to our global simulations.

## 2 Methodology

### 2.1 The SWMF Geospace Model

The SWMF Geospace configuration (Tóth et al., 2012) consists of three coupled models describing the different regimes in the global magnetosphere-ionosophere system (Gombosi et al., 2021).

The Block-Adaptive-Tree-Solarwind-Roe-Upwind-Scheme (BATSRUS) code (Powell et al., 1993) solves the ideal magnetohydrodynamic equations in the solar wind and magnetosphere regions. The grid volumes are variable in the code, it uses Adaptive Mesh Refinement (AMR) to refine the grid size. The highest resolution used for the simulations analyzed in this study was set to 1/8 Earth radii ($R_E$), which is mostly used in the inner magnetosphere and close to the magnetospheric boundaries. The simulation box covers the region around the Earth with the x-axis spanning from -224 $R_E$ in the magnetotail to 32 $R_E$ in the sunward direction, and the y and z-axes span from $-128R_E$ to $128R_E$ in Geocentric Solar Magnetospheric coordinates.

The Rice Convection Model (RCM) is an inner-magnetosphere model primarily used to model the ring current (Wolf, 1983). RCM solves bounce-averaged drift kinetic equations for the particle populations on a polar grid (Toffoletto et al., 2003). RCM is two-way coupled between BATSRUS and the ionosphere. The coupling happens every 10 seconds, where BATSRUS supplies the currents for RCM and RCM in turn returns electric fields for the BATSRUS inner boundary.

The Ridley Ionosphere Model (RIM) is a potential solver for the ionosphere that solves the Poisson equation on a spherical grid (Ridley et al., 2004). It is coupled with RCM and the BATSRUS and uses an empirical conductance model to find the electric field in the ionosphere. The coupling of BATSRUS with RIM happens every 5 seconds where BATSRUS supplies field-aligned currents (FAC). The FACs enable RIM to solve the electric potential using the conductance model.

### 2.2 Simulation Runs

Using the Space Weather Modeling Framework (SWMF) in the Geospace configuration, we ran the same 123 storms introduced in a previous study (Al Shidi et al., 2022).

The storms were selected based on having a minimum peak of stronger than -50 nT during its evolution. Each storm run is 54 hours in total which includes 6 hours before the storm onset time and 48 hours thereafter.

### 2.3 Simulation Inputs

The storms were simulated with SWMF Geospace model using the OMNI solar wind and interplanetary magnetic field (IMF) observations (N. Papitashvili et al., 2014) as input at the simulation Sunward (upstream) boundary. The observations that come from a collection of spacecraft, most of them located at or near the first Lagrangian point L1, are propagated to the nose of the magnetospheric bow shock (BSN) to represent the solar wind and IMF parameters encountered by the Earth's magnetosphere.

In this study, we use the IMF components in GSM coordinates ($B_x$, $B_y$, $B_z$), the solar wind speed ($V$) and density ($n$) to get the solar wind dynamic pressure ($p$), solar wind electric field ($E_y = -VB_z$) and an empirical solar wind – magnetosphere coupling function (Newell et al., 2007)

$$\frac{d\Phi}{dt} = \alpha \left[ v^2 B_T \sin^4 \left( \frac{\theta}{2} \right) \right]^{2/3} \tag{1}$$

where $\theta = \tan^{-1}(B_y/B_z)$ is the IMF clock angle and $B_T = (B_y^2 + B_z^2)^{1/2}$ is the transverse component of the magnetic field perpendicular to the Sun-Earth line. The normalizing factor $\alpha \sim 10^3$ provides conversion to units of Wb/s, which allows interpretation of the parameter as the rate of magnetic flux conversion at the dayside magnetopause (Newell et al., 2007).

The propagation time is determined using the solar wind speed, distance to the observing spacecraft, and by finding a phase front normal (PFN) that describes the orientation of the front that is approaching the Earth (see Figure 1). The PFN can be found using several methods and OMNI employs a combination (King & Papitashvili, 2023) of some of the techniques mentioned in Section 1.

The solar wind front detected at time $t$ at an upstream spacecraft (at location $\boldsymbol{r}_{spacecraft}$) reaches the bow shock nose at time $t + \Delta t$. The transit time $\Delta t$ can be calculated by advecting the phase front normal plane using the equation

$$\Delta t_{arrival} = \frac{(\boldsymbol{r}_{BSN} - \boldsymbol{r}_{spacecraft}) \cdot \hat{\boldsymbol{n}}}{\boldsymbol{V} \cdot \hat{\boldsymbol{n}}}, \tag{2}$$

where $\boldsymbol{r}_{BSN}$ is the location of bow shock nose, $\boldsymbol{V}$ is the solar wind velocity observed at L1, and $\hat{\boldsymbol{n}}$ is the shock phase front normal derived from the solar wind observations at the spacecraft location (see Figure 1 demonstrating the principle of the PFN advection). Errors of this method will arise as well from errors in the solar wind speed, positioning accuracy of the spacecraft, as the evaluation of the PFN orientation.

### 2.4 Simulation Outputs

Each storm simulation was configured to output geomagnetic indices including SYM-H, AL, AU, and the Northern hemisphere polar cap index PCN, which can be used to derive an estimate for the Cross-Polar Cap Potential (CPCP) (Ridley et al., 2004) in the form

$$CPCP = 29.28 - 3.31 \sin(T + 1.49) + 17.81 PCI, \tag{3}$$

where the time of year is specified as $T = 2\pi(N_{MONTH}/12)$ with numbering of months starting from zero (Jan = 0).

To examine the errors in the local geomagnetic field prediction, the simulation output comprises magnetic field perturbations $\Delta \boldsymbol{B}$ at over a hundred ground magnetometer station locations perturbations at 1-minute cadence (Al Shidi & Pulkkinen, 2022).

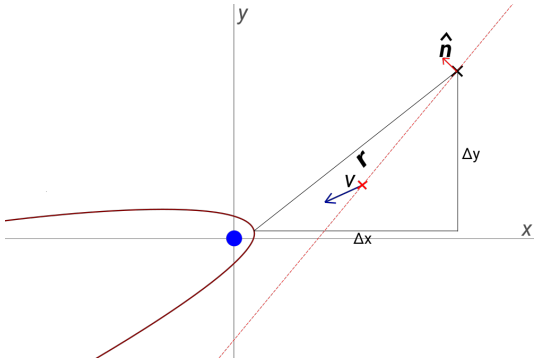


**Figure 1.** A diagram (not to scale) showing a simplified version of how solar wind parameters are propagated from L1. The Earth is shown in blue at the origin of the GSE coordinate system, with the bowshock engulfing the magnetosphere oriented by the direction of the solar wind flow velocity $\boldsymbol{V}$ (blue arrow). The spacecraft situated upstream (black cross) observes a phase front plane (dashed red line; phase front normal $\hat{\boldsymbol{n}}$ is shown with the red arrow) The distance $\boldsymbol{r}$ from the bow shock to the spacecraft has GSE components ($\Delta x$) and ($\Delta y$). The distance of the front plane from the bow shock along the solar wind flow direction is marked with a red $x$. The propagation time from the front plane to the bow shock is then determined by the distance of $x$ to the bow shock and the solar wind speed.

### 2.5 Error Analysis

The observations and simulation outputs are compiled to time series vectors $y_{j,observed}$ and $y_{j,model}$, where $y_j$ is the value of the geomagnetic index $j$ ($j$ = SYM-H, AU, AL, CPCP). The simulation prediction error at time $t_i$ is then defined as

$$\epsilon_j(t_i) = y_{j,\mathrm{model}}(t_i) - y_{j,\mathrm{observed}}(t_i). \tag{4}$$

The error vectors thus created are used to derive probability distributions for the errors under different solar wind driving conditions defined as vectors $z_{k,observed}(t_i)$ at the bow shock nose ($k = E_y$, $d\Phi/dt$, PFN, or the transverse distance from the Sun-Earth line $|\hat{x}\times \boldsymbol{r}|$, $\Delta t$), where $\boldsymbol{r} = \boldsymbol{r}_{spacecraft} - \boldsymbol{r}_{BSN}$.

## 3 Results and Analysis

This study focuses on the magnitude of the errors in the simulation output as compared to the observations for given solar wind input. We note that the solar wind driver parameters used here are not independent, but reflect different characteristics of the incoming solar wind: The intensity of the driving ($E_y$, $d\Phi/dt$), and timing and/or other errors associated with measurements away from the Sun-Earth line and (PFN, $\boldsymbol{y}\cdot\boldsymbol{r}$) and from the bow shock nose ($\Delta t$).

### 3.1 Univariate Analysis

In this section, we examine the probability distributions of the errors for each of the driver parameters. Figures 2, and 3 show the error probability distributions as functions of the driver parameters for each of the activity measures $y_j$. The error distributions are computed for 10 ranges of the driver parameter values, and the figures show the errors normalized for each bin. The error distributions were discretized into 50 bins. Normalization of each driver parameter bin means that the figures do not give the ab-

solute value of the error, but rather a distribution of the error magnitudes within that particular range of the driver parameter.

### *3.1.1 Global Geomagnetic Indices*

The four panels in Figure 2 show the errors in the activity indices CPCP, SYM-H, AL, and AU as function of the intensity of the solar wind electric field $VB_z$ (top row) and the Newell coupling parameter (bottom row). The errors are mostly centered around zero. The errors in the polar cap potential increase slightly both for strong driving (strongly negative $VB_z$) and for strong electric field in a closed magnetosphere configuration (strongly positive $VB_z$). The SYM-H, AL, and AU index errors have widest distributions for strong driving, with SYM-H and AU centered around zero, but the AL errors strongly biased toward negative error (model underestimating the observed AL) typical of the Geospace results (T. I. Pulkkinen et al., 2022). These results are independent of the form of the solar wind coupling function, as can be seen by comparing the top and bottom rows for each of the indices.

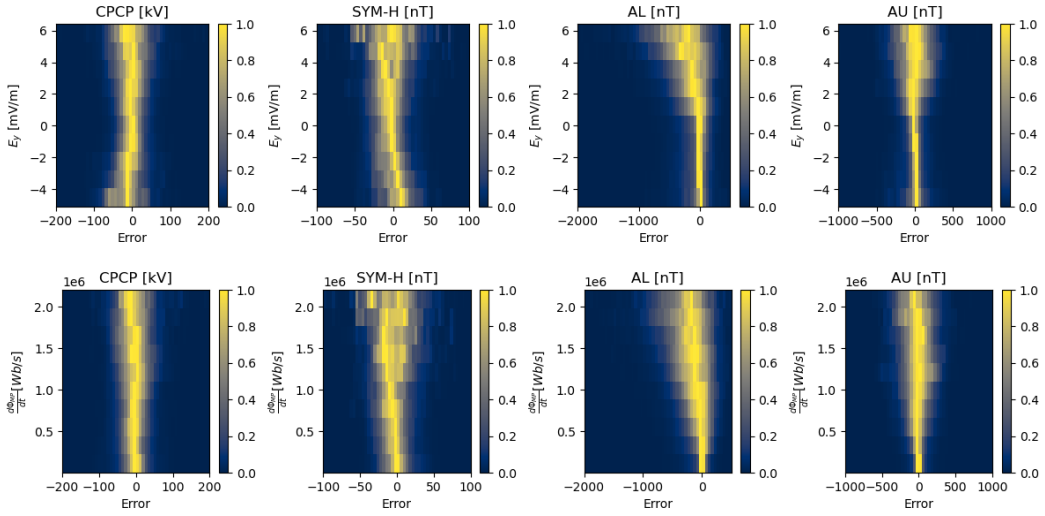


**Figure 2.** From left to right: Binned probability distribution of errors in CPCP, SYM-H, AL and AU as function of the (top) solar wind electric field and (bottom) the Newell coupling function at the bow shock nose. The driver parameters were binned into 10 bins, and the errors into 50 bins.

Examination of the errors of the global indices as a function of PFN (Figure 3) shows less dependence on the phase front orientation than on the solar wind driver function magnitude: The variance and the medians are relatively similar for angles perpendicular and oblique to the sun-earth line (smaller and larger $\hat{\boldsymbol{n}} \cdot \hat{\boldsymbol{x}}$, respectively).

The errors in the geomagnetic indices given the transverse distance of the spacecraft to the BSN show a mostly consistent variance throughout however there is a noticable change in the medians for each given distance. This shows that the error is dependent to the location of the spacecraft but its uncertainty (which could arise from measurement errors) stays the same.

Lastly, we examine the effect of the time shift from the spacecraft to the bow shock nose. Noting that most of the OMNI observations come from spacecraft at or near L1, the higher values of $\Delta t$ imply slower solar wind and the low values imply high solar wind

speed, or, referring to Figure 1, higher values of $\Delta t$ imply close to perpendicular PFN angles and smaller propagation times imply more oblique PFN orientatiton. The errors for all parameters are slightly larger for low time shifts (high solar wind speed, oblique fronts) but especially the polar cap potential and the AU index show very little difference across the range of values in $\Delta t$.

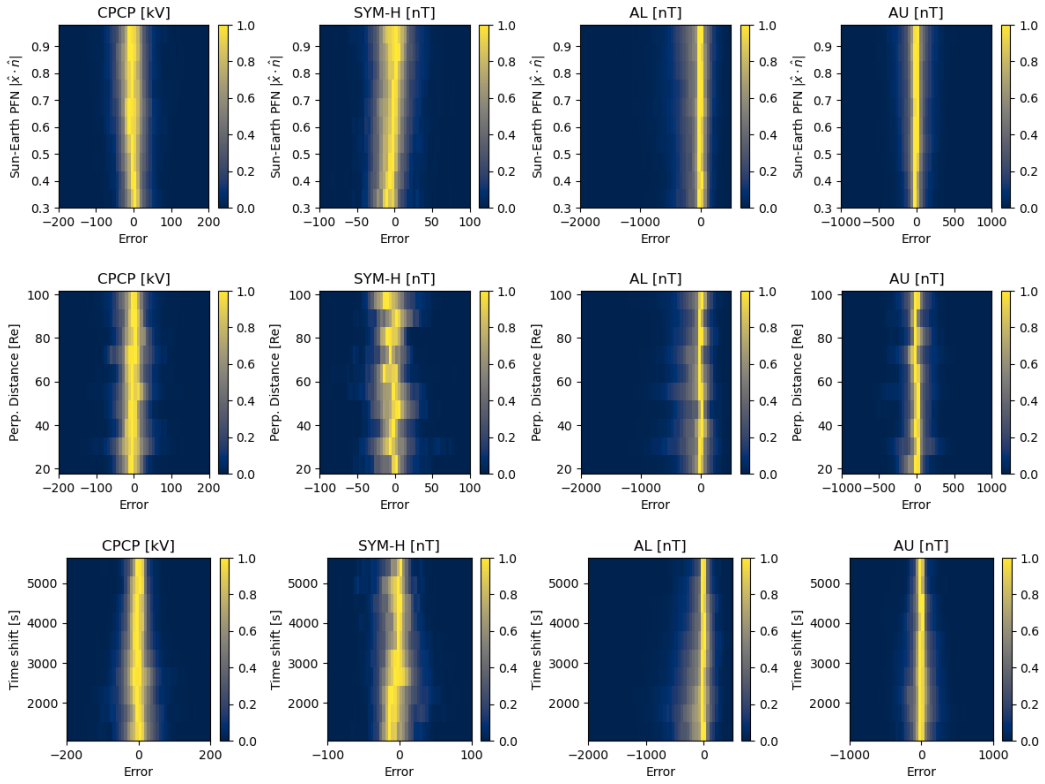


**Figure 3.** From left to right: Binned conditional probability distribution of errors in CPCP, SYM-H, AL and AU as function of the (top) the PFN projection to the $x$ axis ($\hat{x}\cdot\hat{n}$), (middle) the transverse distance from the Sun-Earth line ($|\hat{x}\times r|$), and (bottom) time shift to the bow shock nose $\Delta t$. The driver parameters were binned into 10 bins, and the errors into 50 bins.

To further examine the role of the solar wind parameters, we downsample the inputs to a particular value and show the median error and the interquartile ranges as function of the downsampled distance from the sun-Earth line, the PFN, the solar wind electric field, and the solar wind dynamic pressure (see Figure 4). For the solar wind electric field, dynamic pressure, and the off-axis distance of the BSN to the spacecraft, the subsampling is done by selecting values larger than the value in question. For the PFN the subsampling is done by selecting values smaller than the value in question. These selections are consistent with the assumptions that lower level of solar wind driving (small $E_y$ and $p$), large PFN $\hat{n}\cdot\hat{x}$, and small distance from the Sun-Earth line $|\hat{x}\times r|$ would minimize the errors – consistent with our conclusions above.

The dynamic pressure shows a clear bias in the medians, with the median error decreasing (increasing) for SYM-H (CPCP) for increasing solar wind dynamic pressure. This indicates that the model tends to overestimate the magnitudes of the SYM-H and CPCP for large solar wind pressure values. While the inter-quartile range (IQR) does not much change for SYM-H, it does increase toward higher pressures for the polar cap potential.

For the AL and AU indices, the error distributions get wider for stronger level of driving, and the AL index shows an increasing underestimation of the index values for higher levels of driving. Similar relationship is not found for the flow pressure, which would indicate that the underestimation is dependent on the IMF $B_z$ component rather than the solar wind speed (which is a component of the dynamic pressure).

As the PFN $\hat{n} \cdot \hat{x}$ decreases and the phase fronts become increasingly oblique, the SYM-H distributions get narrower, but at the same time the median errors become more positive, indicating underestimation of the index magnitude. While the IQRs of all parameters decrease slightly for more oblique angles, the other parameters show only slight variations in the median values. The IQR does increase for PFN projection values smaller than 0.2. Since variations in the median and IQR can be seen for values less than 0.4, we can say that we can have more confidence in the geomagnetic indices outputs when the values are greater than 0.4.

The off-axis distance of the spacecraft from the BSN seems to matter for relatively large values, once larger than about 80 $R_E$, changes can be seen in the median and IQR of the errors, where the IQR is show an increase in distances larger than 90 $R_E$.

#### *3.1.2 Local Magnetometer Recordings*

In this subsection, we examine the role of each of the driver parameters in generating errors at individual magnetometer stations. We do that by selecting two representative stations, Yellowknife, Canada (YKC) in the auroral latitudes recording both eastward and westward ionospheric electrojets (Lyatsky et al., 2006), and Boulder, CO, USA (BOU), which is a mid-latitude station mostly reacting to the ring current and field-aligned currents coupling the magnetosphere and ionosphere (Dubyagin et al., 2014). The error vectors computed use the observed and simulated ground magnetic perturbations horizontal to the surface. The four panels in each row of Figure 5 shows the error probability distributions for each of the driver parameters for YKC at the top and BOU at the bottom panel. Note that due to the very different scales of the signals (the auroral zone magnetometers record variations in the 100s of nT, whereas the mid-latitude stations typically record variations of the order of 10s of nT), the horizontal scales are different for the two stations.

The local recordings show similar dependence on the driver parameters than the global indices, although the error distributions in the transverse component are narrower than those of the global indices. Note, however, that for the solar wind driver functions, the horizontal components are not biased toward negative errors, being centered around zero error. Furthernore, BOU shows an increase also for strong driver in the closed magnetosphere configuration (strongly positive $VB_z$). Neither station shows dependence on either the phase front normal or the transverse distance to the Sun-Earth line.

### 3.2 Regression Analysis

In order to study the relationship between the solar wind parameters and the simulation errors, we perform a linear regression analysis to find how the errors change with the varying inputs. Essentially, a linear regression is a least-squares fit to a linear equation:

$$\epsilon_j(t) = b_0 + \sum_k b_k z_k(t), \tag{5}$$

where $\epsilon_j$ is the error associated with the global geomagnetic index $j$, $b_0$ is the y-intercept, $z_k$ is the solar wind quantity $k$ at time $t$, and $b_k$ is the slope or weight associated with the solar wind parameter $k$. We consider the four solar wind parameters introduced earlier, the solar wind electric field $E_y$ and $E_z$, the solar wind dynamic pressure $p$, the PFN projection to the Sun-Earth line $\hat{\boldsymbol{n}} \cdot \hat{\boldsymbol{x}}$, and the observing spacecraft transverse distance

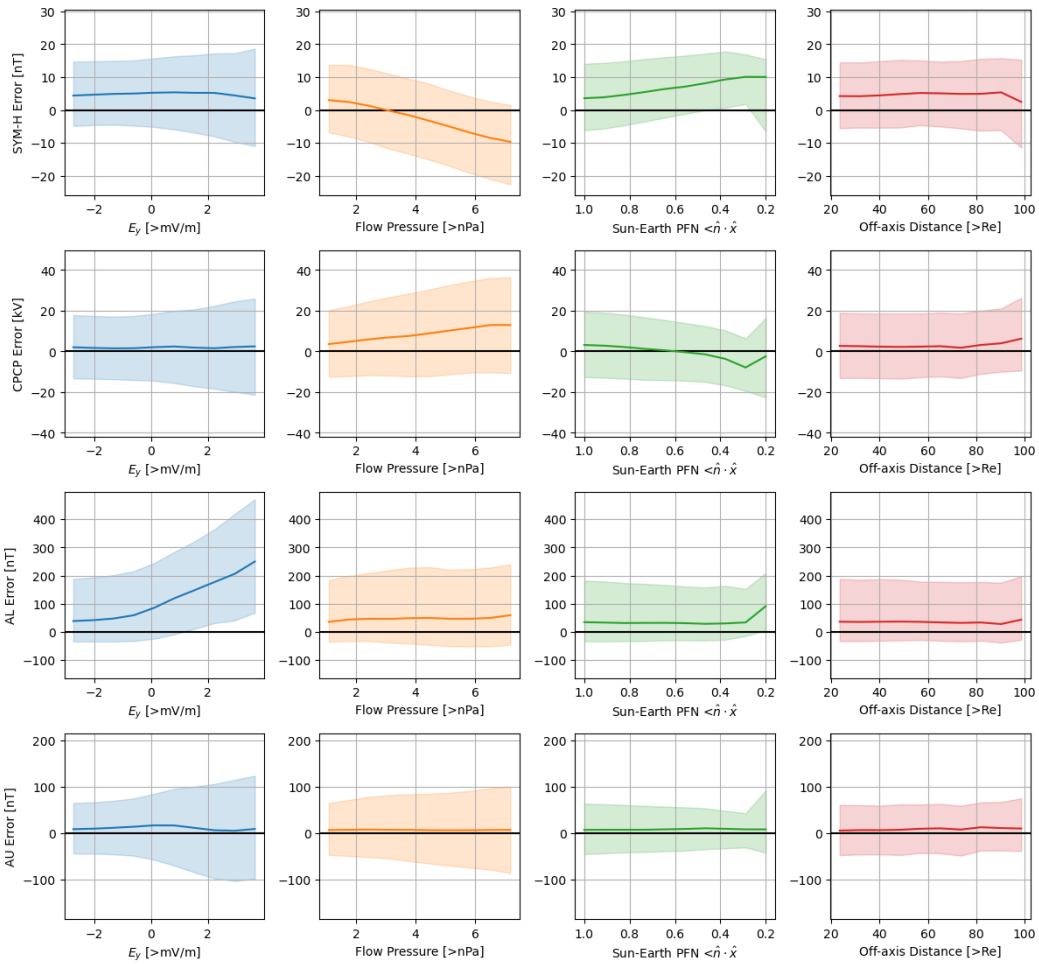


**Figure 4.** Median errors (dark lines) and their inter-quartile ranges (lighter shading) by selectively subsampling the solar wind paramters. From top to bottom, left to right: SYM-H, CPCP, AL, and AU errors as function of the solar wind electric field $E_y$, the solar wind dynamic pressure, the projection of the PFN on the Sun-Earth line, and the transverse (off-axis) distance from the BSN to the spacecraft. For the solar wind electric field, dynamic pressure, and off-axis distance, the subsampling is done by selecting values larger than to the value on the x-axis. For the PFN, the subsampling is done by selecting values smaller than to the value on the x-axis.

from the Sun-Earth line $|\hat{x}\times r|$. As outputs, we consider the same global magnetospheric parameters as before, the SYM-H, the cross-polar cap potential CPCP, and the auroral electrojet indices AL and AU.

To study how large an effect a given solar wind quantity $k$ has on the errors, we calculated Standardized Regression Coefficients (SRC) for each geomagnetic activity parameter $j$ using the formulation

$$\mathrm{SRC}_{jk} = \frac{\sigma_k}{\sigma_j} b_k, \tag{6}$$

where $\sigma$ is the standard deviation of the solar wind parameters $k$ or activity index errors $j$. The SRC is a measure of how much of the variance in the errors can be attributed to the variance in the inputs. This allows us to make a relational inference between the solar wind inputs and activity index errors, and to directly compare across the param-

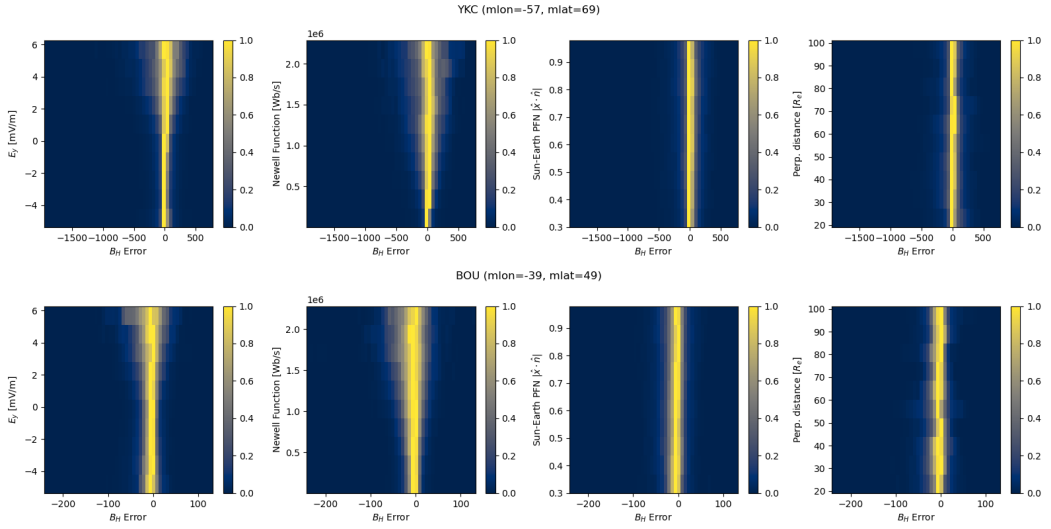


**Figure 5.** From left to right: Binned probability distribution of errors the horizontal magnetic field at (top) YKC and (bottom) BOU as function of the solar wind $E_y$, the Newell coupling function, the PFN projection to the $x$ axis ($\hat{x} \cdot \hat{n}$), and the transverse distance from the Sun-Earth line ($|\hat{x} \times r|$). The driver parameters were binned into 10 bins, and the errors into 50 bins.

eters as the SRC are unitless. Table 1 shows the SRCs found for each solar wind input and geomagnetic index error.

**Table 1.** Table of the Standardized Regression Coefficients

| Error | $\lvert\hat{x} \times r\rvert$ | PFN $\hat{\boldsymbol{n}} \cdot \hat{\boldsymbol{x}}$ | $VB_y$ | $VB_z$ | Pressure $p$ |
|---|---|---|---|---|---|
| SYM-H | 0.077 | 0.123 | 0.017 | 0.153 | 0.293 |
| CPCP | 0.018 | 0.105 | 0.095 | 0.109 | 0.071 |
| AL | 0.005 | 0.0179 | 0.312 | 0.294 | 0.098 |
| AU | 0.021 | 0.013 | 0.480 | 0.066 | 0.008 |

The SRC's show that the variances in SYM-H are sensitive to the variances in the PFN and $VB_z$ equally and doubly so for the solar wind pressure. The variances in CPCP are equally sensitive to PFN, $VB_y$, and $VB_z$ but less so to the solar wind pressure. The variances in the AL errors are even more sensitive (triply so) to the solar wind electric field analogues $VB_z$ and $VB_y$ with an even less sensitive relationship to variances in the PFN. The less sensitive variance relationship to PFN can also be seen in AU error, but interestingly, AU is sensitive to variances in $VB_y$ strongly and less so on $VB_z$.

## 4 Discussion

This study focuses on the analysis of the magnitude and probability distribution of errors between observations of geomagnetic indices and their predictions using the Space Weather Modeling Framework Geospace simulation. The errors can arise either from inaccuracies in the measurement (measurement errors), errors in the predicted magnitude with the correct driver profile (model error), or errors in timing of the arrival of the solar wind and IMF at the bow shock nose.

Further investigations into the cause of the errors would require better metadata for the observational inputs and outputs: Neither the geomagnetic indices nor the space-borne solar wind measurements and propagation times come with uncertainty estimates or error bars. Such parameters would be necessary to understand how the uncertainties propagate from the input to the output measurements, and would be valuable for uncertainty quantification and validation of space weather forecasts. Lacking these, Morley et al. (2018) attempted to quantify the uncertainty of measurement errors in the solar wind input by ensemble modeling with SWMF, and showed that using ensemble modeling can improve the mean error of SYM-H by a few nT.

Our results show that the errors show only minor dependence on the geometric parameters such as the phase front normal angle or the transverse distance from the Sun-Earth line of the observing spacecraft, while the widest distributions of the errors are obtained for large solar wind driving and high dynamic pressure. An earlier study by Ridley (2000) demonstrated that the uncertainty in timing between measurements at L1 with WIND and closer to the BSN with IMP 8 can be on average 7.5–8.5 minutes. However, their study was limited to the solar wind, and did not assess the impact of these timing errors on the errors in geomagnetic indices, which have their own intrinsic time scales as they respond to the variable solar wind driving. More recently, Milan et al. (2022) found that the correlation of peaks in the cusp R0 field-aligned currents observed by the AMPERE satellites with IMF $B_y$ deteriorates with larger transverse distance of the solar wind monitor from the Sun-Earth line. Furthermore, they find an average time lag of about 17 minutes between the solar wind front arrival at the bow shock nose and the response caused by the front in the ionosphere – irrespective of the location of the solar wind monitor, a physics based simulation is expected to have the same response time which makes the minute cadence comparison fair.

A limitation of the regression analysis performed in Section 3.2 is the non-linear relationship between the solar wind inputs and the geomagnetic index errors. The value of the regression analysis is in its ability to address the relationship between the variances of both input and output simultaneously, characterized by the standardized regression coefficients.

## 5 Conclusion

The errors in the prediction of geomagnetic indices are dominated by the energy of the solar wind interacting with the magnetosphere, shown as increasing interquartile range of the errors for higher levels of solar wind driving (larger electric field, Newell coupling parameter, or solar wind dynamic pressure). Propagation methods used to propagate the solar wind from L1 to the BSN show less significant effects, however, smaller phase front normal angles with respect to the Sun-Earth line show slightly smaller uncertainties (smaller interquartile range) than larger angles. The transverse distance of the solar wind monitor from the Sun-Earth line shows little effect on the geomagnetic index error, although we note that timing errors in these cases might be dominant.

## 6 Open Research

The data used in this study is openly available in the Deep Blue Data repository (Al Shidi & Pulkkinen, 2022) and can be retrieved from: `https://doi.org/10.7302/dkjd-1j05`. The geomagnetic indices and solar wind data are aggregated in the OMNI dataset (N. E. Papitashvili & King, 2020) and can be found here: `https://omniweb.gsfc.nasa.gov/` .

## Acknowledgments

This research was funded by NASA grant 80NSSC21K1753 and NSF grant 2033563.

## References

Al Shidi, Q., & Pulkkinen, T. (2022). *Space weather modeling framework simulations of ground magnetometer data [dataset]* [dataset]. University of Michigan - Deep Blue Data. Retrieved from https://doi.org/10.7302/dkjd-1j05 doi: 10.7302/dkjd-1j05

Al Shidi, Q., Pulkkinen, T., Toth, G., Brenner, A., Zou, S., & Gjerloev, J. (2022). A Large Simulation Set of Geomagnetic Storms—Can Simulations Predict Ground Magnetometer Station Observations of Magnetic Field Perturbations? *Space Weather*, *20*(11), e2022SW003049. Retrieved 2023-01-24, from https://onlinelibrary.wiley.com/doi/abs/10.1029/2022SW003049 (_eprint: https://onlinelibrary.wiley.com/doi/pdf/10.1029/2022SW003049) doi: 10.1029/2022SW003049

Cash, M., Singer, H., Millward, G., Adamson, E., Balch, C., Welling, D., & Toth, G. (2018). NOAA/SWPC OPERATIONAL MODEL PERFORMANCE DURING THE SEPTEMBER 2017 STORMS. *Space Weather Workshop*. Retrieved from https://www.swpc.noaa.gov/sites/default/files/images/u4/04\%20Michele\%20Cash.pdf

Dubyagin, S., Ganushkina, N., Kubyshkina, M., & Liemohn, M. (2014). Contribution from different current systems to sym and asy midlatitude indices. *Journal of Geophysical Research: Space Physics*, *119*(9), 7243-7263. Retrieved from https://agupubs.onlinelibrary.wiley.com/doi/abs/10.1002/2014JA020122 doi: https://doi.org/10.1002/2014JA020122

Gombosi, T. I., Chen, Y., Glocer, A., Huang, Z., Jia, X., Liemohn, M. W., ... Zou, S. (2021, May). What sustained multi-disciplinary research can achieve: The space weather modeling framework. *Journal of Space Weather and Space Climate*, *11*, 42. (_eprint: 2105.13227) doi: 10.1051/swsc/2021020

Horbury, T. S., Burgess, D., Fränz, M., & Owen, C. J. (2001). Prediction of earth arrival times of interplanetary southward magnetic field turnings. *Journal of Geophysical Research: Space Physics*, *106*(A12), 30001-30009. Retrieved from https://agupubs.onlinelibrary.wiley.com/doi/abs/10.1029/2000JA002232 doi: https://doi.org/10.1029/2000JA002232

Janhunen, P., Palmroth, M., Laitinen, T., Honkonen, I., Juusola, L., Facskó, G., & Pulkkinen, T. (2012). The gumics-4 global mhd magnetosphere–ionosphere coupling simulation. *Journal of Atmospheric and Solar-Terrestrial Physics*, *80*, 48-59. Retrieved from https://www.sciencedirect.com/science/article/pii/S1364682612000909 doi: https://doi.org/10.1016/j.jastp.2012.03.006

King, J., & Papitashvili, N. (2023). NASA SPDF. Retrieved from https://omniweb.gsfc.nasa.gov/html/HROdocum.html#3a

Lyatsky, W., Tan, A., & Lyatskaya, S. (2006). Monitoring the auroral electrojet from polar cap stations. *Journal of Geophysical Research: Space Physics*, *111*(A7). Retrieved from https://agupubs.onlinelibrary.wiley.com/doi/abs/10.1029/2004JA010989 doi: https://doi.org/10.1029/2004JA010989

Lyon, J. G., Fedder, J. A., & Mobarry, C. M. (2004). The Lyon-Fedder-Mobarry (LFM) global MHD magnetospheric simulation code. *J. Atmos. Sol-Terr. Phys.*, *66*, 1333.

Milan, S. E., Carter, J. A., Bower, G. E., Fleetham, A. L., & Anderson, B. J. (2022). Influence of off-sun-earth line distance on the accuracy of l1 solar wind monitoring. *Journal of Geophysical Research: Space Physics*, *127*(6), e2021JA030212. Retrieved from https://agupubs.onlinelibrary.wiley.com/doi/abs/10.1029/2021JA030212 (e2021JA030212 2021JA030212) doi: https://doi.org/10.1029/2021JA030212

Morley, S. K., Welling, D. T., & Woodroffe, J. R. (2018). Perturbed Input Ensemble

Modeling With the Space Weather Modeling Framework. *Space Weather*, *16*, 1330. doi: 10.1029/2018SW002000

Newell, P. T., Sotirelis, T., Liou, K., Meng, C. I., & Rich, F. J. (2007, January). A nearly universal solar wind-magnetosphere coupling function inferred from 10 magnetospheric state variables. *Journal of Geophysical Research*, *112*, 01206.

Papitashvili, N., Bilitza, D., & King, J. (2014, January). OMNI: A Description of Near-Earth Solar Wind Environment. In *40th COSPAR Scientific Assembly, 2-10 August, 2014, Moscow, Russia* (Vol. 40, pp. C0.1–12–14).

Papitashvili, N. E., & King, J. H. (2020). *Omni 1-min data.* NASA Space Physics Data Facility. doi: 10.48322/45bb-8792

Powell, K. G., Roe, P. L., & J. Quirk. (1993). Adaptive-mesh algorithms for computational fluid dynamics. In M. Y. Hussaini, A. Kumar, & M. D. Salas (Eds.), *Algorithmic Trends in Computational Fluid Dynmaics* (pp. 303–337). New York: Springer-Verlag.

Pulkkinen, A., & Rastätter, L. (2009). Minimum variance analysis-based propagation of the solar wind observations: Application to real-time global magnetohydrodynamic simulations. *Space Weather*, *7*, 12011. doi: 10.1029/2009SW000468

Pulkkinen, T. I., Brenner, A., Al Shidi, Q., & Toth, G. (2022). Statistics of geomagnetic storms: Global simulations perspective. *Frontiers in Astronomy and Space Sciences*, *9*. Retrieved from `https://www.frontiersin.org/articles/10.3389/fspas.2022.972150` doi: 10.3389/fspas.2022.972150

Ridley, A. J. (2000). Estimation of the uncertainty in timing the relationship between magnetospheric and solar wind processes. *J. Atmos. Sol-Terr. Phys.*, *62*, 757.

Ridley, A. J., Gombosi, T. I., & Zeeuw, D. L. D. (2004). Ionospheric control of the magnetospheric configuration: Conductance. *Ann. Geophys.*, *22*, 567–584.

Sonnerup, B., & Scheible, M. (1998). Analysis methods for multi-spacecraft data. *ISSI Scientific Report*.

Toffoletto, F., Sazykin, S., Spiro, R., & Wolf, R. (2003). Inner magnetospheric modeling with the Rice Convection Model. *Space Sci. Rev.*, *107*, 175–196. doi: 10.1023/A:1025532008047

Tóth, G., Holst, B. v. d., Sokolov, I. V., Zeeuw, D. L. D., Gombosi, T. I., Fang, F., ... Opher, M. (2012). Adaptive Numerical Algorithms in Space Weather Modeling. *J. Comput. Phys.*, *231*(3), 870–903. doi: 10.1016/j.jcp.2011.02.006

Weimer, D. R., & King, J. H. (2008). Improved calculations of interplanetary magnetic field phase front angles and propagation time delays. *Journal of Geophysical Research: Space Physics*, *113*(A1). Retrieved from `https://agupubs.onlinelibrary.wiley.com/doi/abs/10.1029/2007JA012452` doi: https://doi.org/10.1029/2007JA012452

Wolf, R. A. (1983, January). Computer Model of Inner Magnetospheric Convection. In R. L. Carovillano & J. M. Forbes (Eds.), *Solar-Terrestrial Physics: Principles and Theoretical Foundations* (Vol. 104, p. 342). doi: 10.1007/978-94-009-7194-3_14

**Figure 1.**

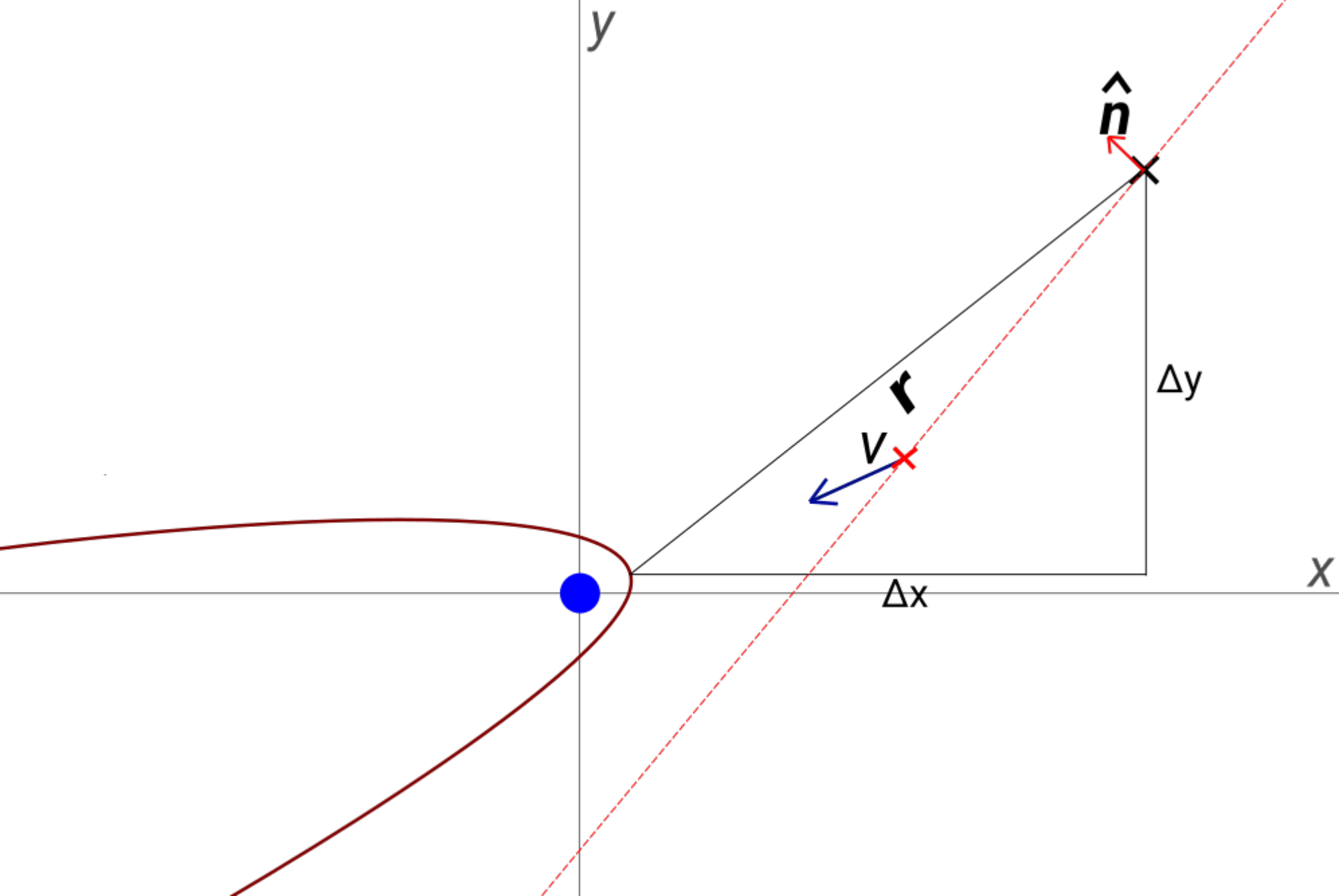
y
x
$\hat{n}$
r
v
Δy
Δx

**Figure 2.**

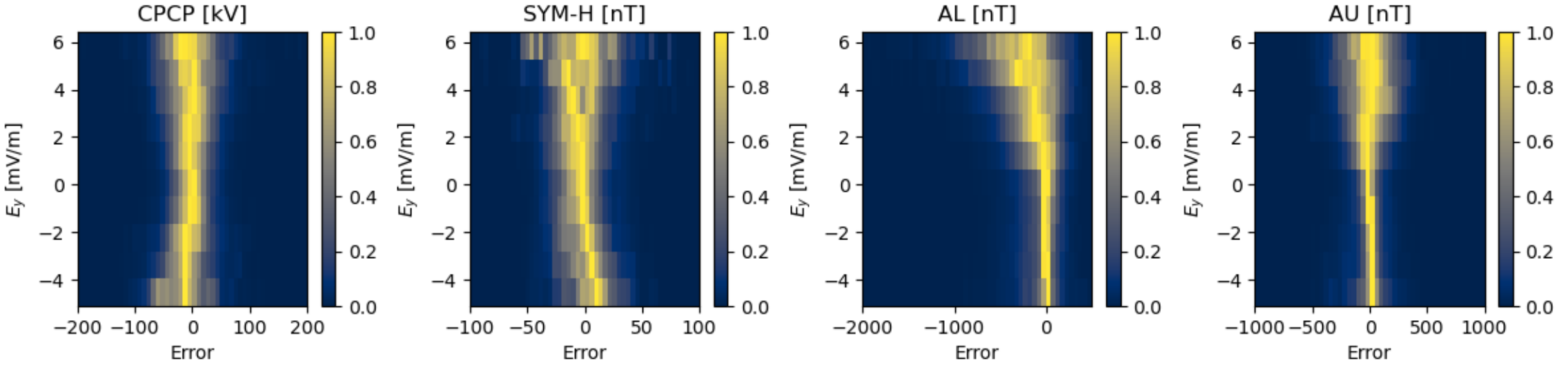
CPCP [kV]
SYM-H [nT]
AL [nT]
AU [nT]
$E_y$ [mV/m]
Error
6
4
2
0
−2
−4
−200 −100 0 100 200
−100 −50 0 50 100
−2000 −1000 0
−1000 −500 0 500 1000
1.0
0.8
0.6
0.4
0.2
0.0

**Figure 2.**

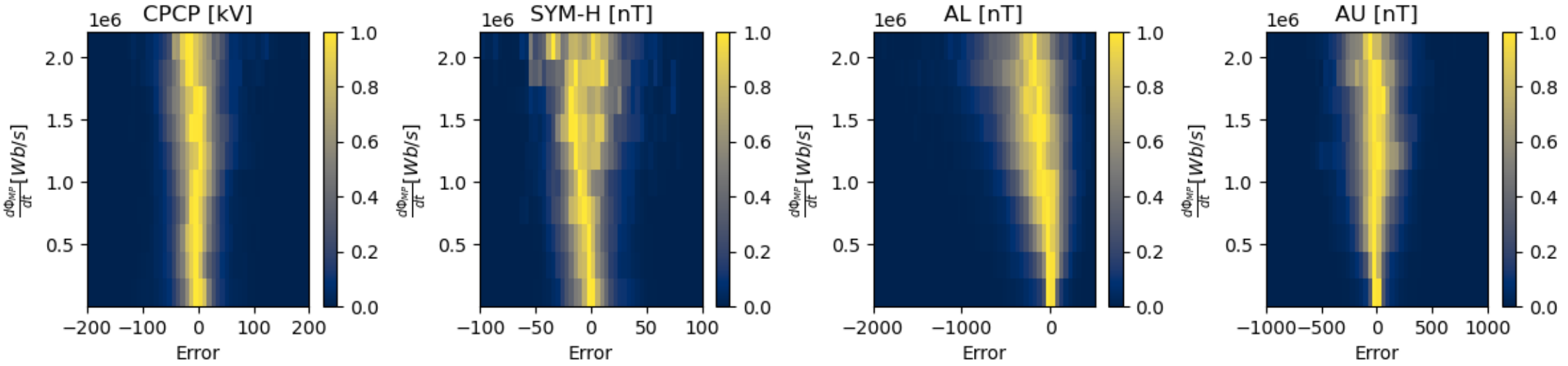
CPCP [kV]
SYM-H [nT]
AL [nT]
AU [nT]
1e6
$\frac{d\Phi_{MP}}{dt}[Wb/s]$
Error
2.0
1.5
1.0
0.5
1.0
0.8
0.6
0.4
0.2
0.0
−200 −100 0 100 200
−100 −50 0 50 100
−2000 −1000 0
−1000 −500 0 500 1000

**Figure 3.**

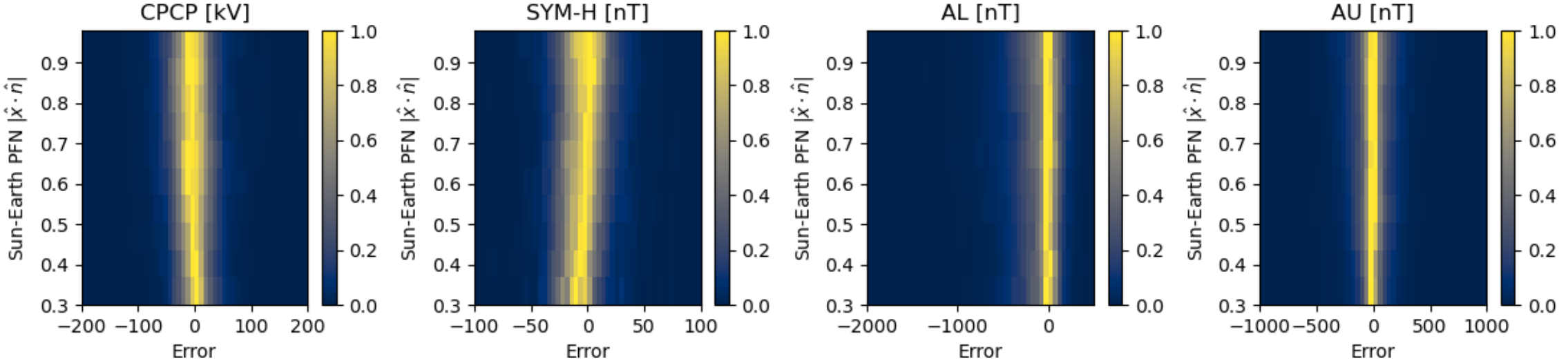
CPCP [kV]
SYM-H [nT]
AL [nT]
AU [nT]
Sun-Earth PFN $|\hat{x} \cdot \hat{n}|$
Error
0.3
0.4
0.5
0.6
0.7
0.8
0.9
1.0
0.0
0.2
0.4
0.6
0.8
1.0
−200 −100 0 100 200
−100 −50 0 50 100
−2000 −1000 0
−1000 −500 0 500 1000

**Figure 3.**

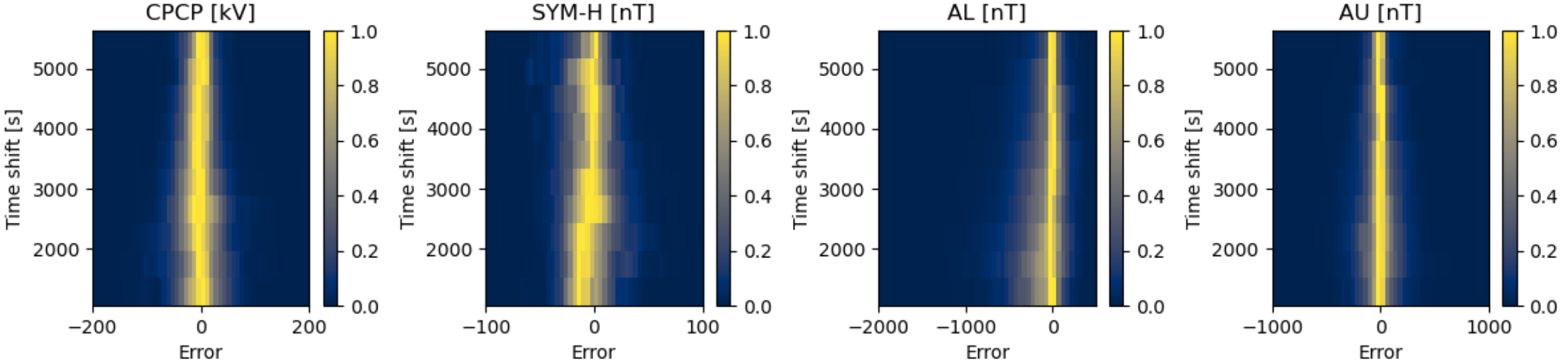
CPCP [kV]
SYM-H [nT]
AL [nT]
AU [nT]
Time shift [s]
Error
5000
4000
3000
2000
−200
0
200
−100
100
−2000
−1000
−1000
1000
1.0
0.8
0.6
0.4
0.2
0.0

**Figure 3.**

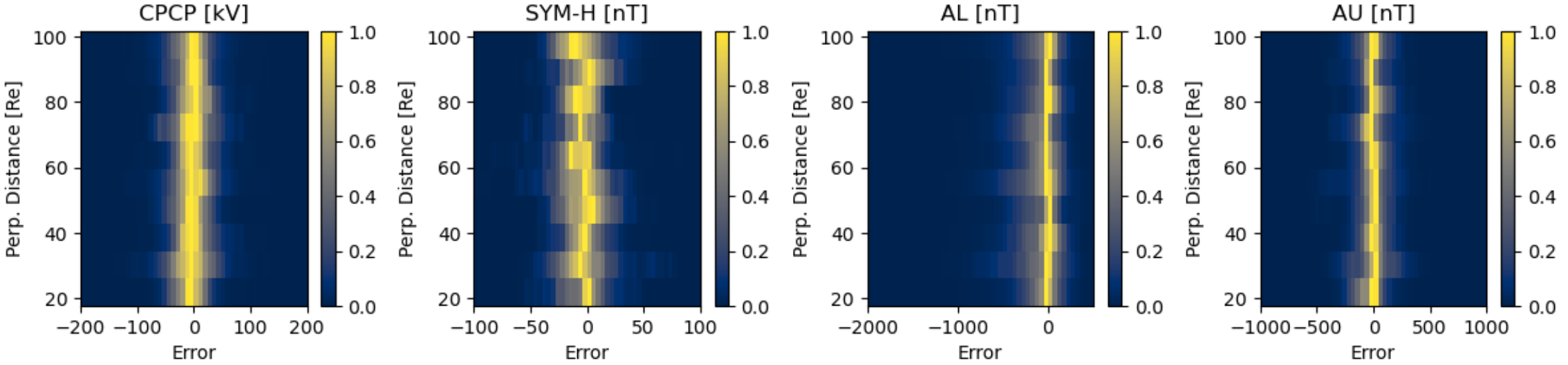
CPCP [kV]
SYM-H [nT]
AL [nT]
AU [nT]
Perp. Distance [Re]
Error
100
80
60
40
20
−200 −100 0 100 200
−100 −50 0 50 100
−2000 −1000 0
−1000 −500 0 500 1000
1.0
0.8
0.6
0.4
0.2
0.0

**Figure 4.**

SYM-H Error [nT]
CPCP Error [kV]
AL Error [nT]
AU Error [nT]
$E_y$ [>mV/m]
Flow Pressure [>nPa]
Sun-Earth PFN $<\hat{n}\cdot\hat{x}$
Off-axis Distance [>Re]

**Figure 5.**

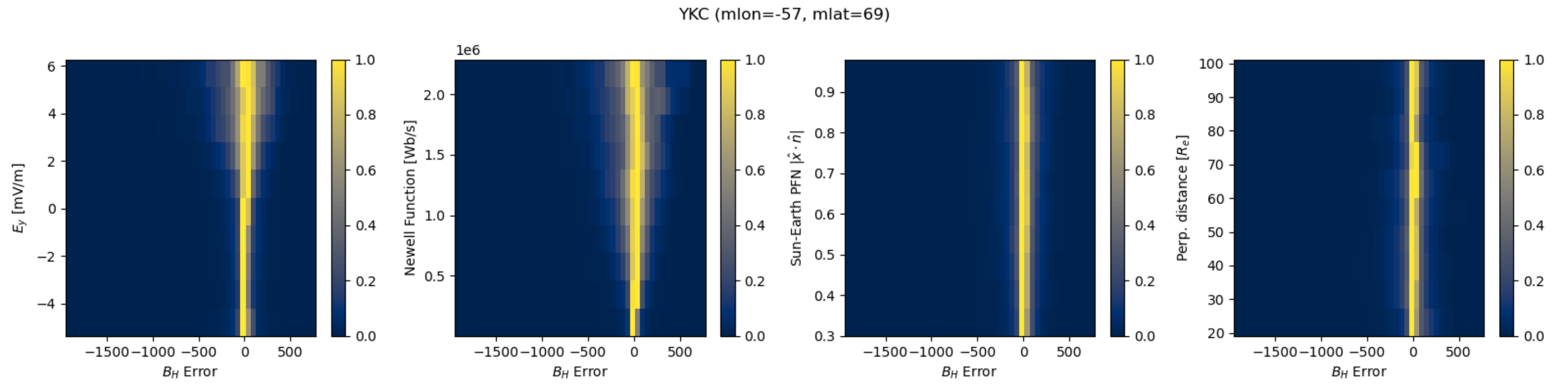
YKC (mlon=-57, mlat=69)
$E_y$ [mV/m]
Newell Function [Wb/s]
1e6
Sun-Earth PFN $|\hat{x} \cdot \hat{n}|$
Perp. distance [$R_e$]
$B_H$ Error
$B_H$ Error
$B_H$ Error
$B_H$ Error

**Figure 5.**

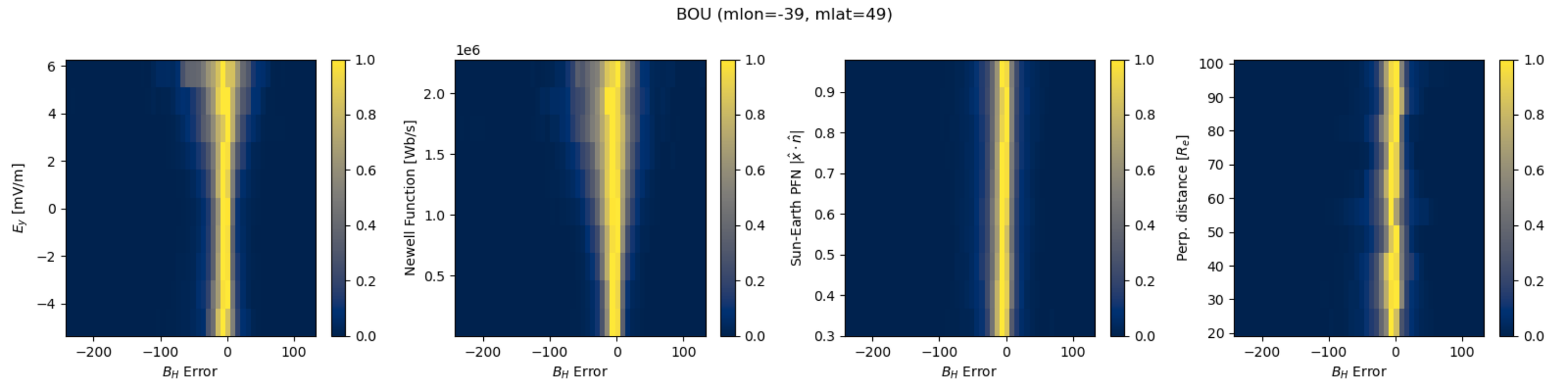
BOU (mlon=-39, mlat=49)
$E_y$ [mV/m]
Newell Function [Wb/s]
1e6
Sun-Earth PFN $|\hat{x} \cdot \hat{n}|$
Perp. distance [$R_e$]
$B_H$ Error
$B_H$ Error
$B_H$ Error
$B_H$ Error